Nano Research 2016, 9(7): 2110–2122
DOI 10.1007/s12274-016-1101-2
Research Article
ISSN 1998-0124
CN 11-5974/O4

Spinel $MnCo_2O_4$ nanoparticles cross-linked with two-dimensional porous carbon nanosheets as a high-efficiency oxygen reduction electrocatalyst

Gengtao Fu[1,3,§], Zhenyuan Liu[1,§], Jingfei Zhang[1], Jiayan Wu[1], Lin Xu[1], Dongmei Sun[1], Jubing Zhang[1], Yawen Tang[1] (✉), and Pei Chen[2] (✉)

[1] *Jiangsu Key Laboratory of New Power Batteries, Jiangsu Collaborative Innovation Centre of Biomedical Functional Materials, School of Chemistry and Materials Science, Nanjing Normal University, Nanjing 210023, China*
[2] *Key Laboratory of Applied Surface and Colloid Chemistry (MOE), School of Materials Science and Engineering, Shaanxi Normal University, Xi'an 710062, China*
[3] *Materials Science and Engineering Program & Texas Materials Institute, the University of Texas at Austin, Austin, Texas 78712, USA*
[§] *These authors contributed equally to this work.*

Received: 25 January 2016
Revised: 18 March 2016
Accepted: 14 April 2016

KEYWORDS
spinel $MnCo_2O_4$,
carbon,
porous nanosheets,
electrocatalysis,
oxygen reduction reaction

ABSTRACT

Catalysts for the oxygen reduction reaction (ORR) play an important role in fuel cells. Alternative non-precious metal catalysts with comparable ORR activity to Pt-based catalysts are highly desirable for the development of fuel cells. In this work, we report for the first time a spinel $MnCo_2O_4$/C ORR catalyst consisting of uniform $MnCo_2O_4$ nanoparticles cross-linked with two-dimensional (2D) porous carbon nanosheets (abbreviated as porous $MnCo_2O_4$/C nanosheets), in which glucose is used as the carbon source and NaCl as the template. The obtained porous $MnCo_2O_4$/C nanosheets present the combined properties of an interconnected porous architecture and a large surface area (175.3 $m^2 \cdot g^{-1}$), as well as good electrical conductivity (1.15×10^2 $S \cdot cm^{-1}$). Thus, the as-prepared $MnCo_2O_4$/C nanosheets efficiently facilitate electrolyte diffusion and offer an expedite transport path for reactants and electrons during the ORR. As a result, the as-prepared porous $MnCo_2O_4$/C nanosheet catalyst exhibits enhanced ORR activity with a higher onset potential and current density than those of its counterparts, including pure $MnCo_2O_4$, carbon nanosheets, and Vulcan XC-72R carbon. More importantly, the porous $MnCo_2O_4$/C nanosheets exhibit a comparable electrocatalytic activity but superior stability and tolerance toward methanol crossover effects than a high-performance Pt/C catalyst in alkaline medium. The synthetic strategy outlined here can be extended to other non-precious metal catalysts for application in electrochemical energy conversion.

Address correspondence to Yawen Tang, tangyawen@njnu.edu.cn; Pei Chen, chenpei@snnu.edu.cn

1 Introduction

With the ever increasing consumption of energy and the impending depletion of traditional fossil fuels, there is a strong need for new energy production and storage technologies. Fuel cells, as green and efficient alternative energy sources, have drawn a great deal of attention [1, 2]. Efficient catalysts for the oxygen reduction reaction (ORR) play a crucial role in the development of fuel cells [3–8]. To date, Pt has displayed the highest reported activity for the ORR with a high onset potential and current density in alkaline medium, but its high cost, scarcity, poor stability, and sluggish ORR kinetics have restricted its use in practical applications. Therefore, there is a need to identify alternative, low-cost, and environmentally benign Pt-free catalysts for the ORR [9–12].

This search has been confined to transition metal oxides. In 1973, MnO_2 was reported to be active in the ORR [13]. Spinel oxides (AB_2O_4), which are built around a closely packed array of O^{2-} ions with A^{2+} and B^{3+} cations occupying part or all of the tetrahedral and octahedral sites [14], are known to be low-cost, active catalysts in the ORR [15–17]. More recently, Wang and co-workers reported a facile precursor pyrolysis method to prepare porous spinel-type $CoMn_2O_4$ and $MnCo_2O_4$ nanoparticles, which exhibited excellent ORR activity along with high stability [16]. Since AB_2O_4 spinels are semiconductors and highly active catalysts require good electrical conductivity, AB_2O_4 spinel nanoparticles require attachment to a conductive substrate. Carbon materials, such as graphene, carbon black, and carbon nanotubes, have been widely used as substrates to supplement the inadequate conductivity of metal oxides [15, 17–19]. For example, Dai and co-workers demonstrated that a $MnCo_2O_4$/N-graphene hybrid could outperform the ORR current density of a Pt/C catalyst at intermediate overpotentials [17]. However, catalysts supported on graphene are easily isolated inside the stacked layers or sandwiched between aggregated graphene sheets and, thus, are not available for the ORR. As for carbon black or carbon nanotubes, the catalysts supported on their external surface easily peel off due to the weak interaction between the catalyst and the carbon substrate. Consequently, it remains a challenge to develop a simple and effective method to prepare catalysts supported on desired carbon substrates for ORR catalysis.

In addition, the ORR performance of catalysts also depends highly on their surface or interface structure. Specifically, nanostructured electrodes with porous configuration and large surface area can greatly improve the electrode/electrolyte contact area and shorten the diffusion path of current carriers, hence enhancing the mass and electron transport [20–24]. Thus, many efforts have been devoted toward the development of porous nanostructures for ideal ORR electrocatalysts, including $MnCo_2O_4$ anchored on P-doped porous carbon [25], carbon-coated $BaMnO_3$ porous nanorods [26], Fe/Fe_3C-functionalized melamine foam [27], mesoporous N-doped graphene [28], etc. Despite the tremendous progress in spinel oxides for the ORR in recent time, the development of a convenient, economical, and scalable approach to prepare spinel ORR catalysts with interconnecting porous structures is still urgently required.

Herein, we have designed and synthesized a novel $MnCo_2O_4$/C nanosheet catalyst consisting of uniform $MnCo_2O_4$ nanoparticles cross-linked with two-dimensional (2D) porous carbon nanosheets with superior electrochemical performance for the ORR in alkaline medium. With the assistance of a NaCl template, the 2D porous $MnCo_2O_4$/C nanosheets can be synthesized *in situ* using $Mn(Ac)_2$ and $Co(Ac)_2$ as metal precursors and glucose as the carbon source. Since the as-obtained 2D porous nanosheets possess several remarkable features, such as high porosity, large surface area (175.3 $m^2 \cdot g^{-1}$), and good electrical conductivity (1.15×10^2 $S \cdot cm^{-1}$), these nanostructures effectively facilitate electrolyte diffusion and offer an expedite transport path for reactants and electrons during the ORR. As a result, the non-precious $MnCo_2O_4$/C nanosheets display excellent activity for the ORR in terms of electrocatalytic activity, long-term stability, and excellent resistance to methanol crossover effects.

2 Experimental

2.1 Reagents and chemicals

All chemicals were procured from either Alfa Aesar

or Sigma Aldrich in their highest purity form available. Pt/C (20 wt.%) was purchased from Johnson Matthey Chemicals Ltd. Vulcan XC-72R carbon was obtained from the America Cobot company. All reagents and chemicals were used as received without further purification.

2.2 Synthesis of porous $MnCo_2O_4$/C nanosheets

In a typical synthesis, a mixture of 1.8 g of glucose ($C_6H_{12}O_6$), 245 mg of manganese(II) acetate tetrahydrate ($Mn(Ac)_2{\cdot}4H_2O$), 498 mg of cobalt(II) acetate tetrahydrate ($Co(Ac)_2{\cdot}4H_2O$), and 8.0 g of NaCl was ground for 1 h with an agate mortar-pestle set. Subsequently, 10.0 mL of deionized water was added to the sample mixture to dissolve $Mn(Ac)_2$, $Co(Ac)_2$, and glucose. After stirring for 30 min, the resultant mixture was dried at 40 ℃ for 10 h and then heated at 750 ℃ for 6 h under Ar atmosphere. The obtained product was further heated at 300 ℃ for 4 h in air to obtain the final crystalline phase ($MnCo_2O_4$/C). Once cooled down to room temperature, the obtained puffy product was washed with water and absolute alcohol several times to remove the NaCl, and then dried at 60 ℃.

For comparison purposes, pure $MnCo_2O_4$ was prepared by further annealing the $MnCo_2O_4$/C sample at 600 ℃ for 6 h in air. Pure carbon nanosheets were achieved by immersing the $MnCo_2O_4$/C nanosheets in an HCl solution (1 M) for 10 h to dissolve the $MnCo_2O_4$ nanoparticles.

2.3 Electrochemical measurements

The electrodes were prepared by drop-casting ink containing the catalyst powder on a glassy carbon electrode. Typically, 5 mg of the sample was sonicated in a mixture of 1.9 mL ethanol and 100 μL neutralized Nafion (5 wt.%, Sigma-Aldrich) for 30 min to form a homogeneous catalyst ink. The catalyst ink was then coated onto a rotating disk electrode (RDE, 0.196 cm^2) at a loading of 10 μL, and dried at room temperature (loading density of ~127.5 $\mu g{\cdot}cm^{-2}$). All electrochemical tests were performed with a Ag/AgCl (1 M NaCl) electrode as the reference electrode and a platinum wire counter electrode at a scan rate of 5 $mV{\cdot}s^{-1}$ in an O_2-saturated 0.1 M KOH solution. All electrochemical tests were performed on Autolab Electrochemical Instrumentation equipped with high-speed rotators from Pine Instruments. All potentials are reported versus the reversible hydrogen electrode (RHE), and the following equation was used for the conversion of the obtained potential (vs. Ag/AgCl) to the RHE: $E_{RHE} = E_{Ag/AgCl} + 0.0592pH + E^0_{Ag/AgCl}$ [$E^0_{Ag/AgCl}$ (in 1 M KCl) = +0.235 V, pH = 12.9 for 0.1 M KOH].

The overall electron transfer number per oxygen molecule involved in the typical ORR process was calculated from the slope of the Koutecky–Levich plots using the following equations [29]

$$\frac{1}{J} = \frac{1}{J_L} + \frac{1}{J_K} = \frac{1}{B\omega^{1/2}} + \frac{1}{J_K} \quad (1)$$

$$B = 0.62nFC_0D_0^{2/3}\upsilon^{-1/6} \quad (2)$$

where J is the measured current density, J_K and J_L are the kinetic and diffusion-limiting current densities, ω is the angular velocity, n is the electron transfer number, F is the Faraday constant (F = 96,485 $C{\cdot}mol^{-1}$), C_0 is the concentration of O_2 (1.2×10^{-3} M), D_0 is the diffusion coefficient of O_2 (1.9×10^5 $cm^2{\cdot}s^{-1}$), υ is the kinematic viscosity of the electrolyte (0.01 $cm^2{\cdot}s^{-1}$). The constant value 0.62 in Eq. (2) is substituted by 0.2 when the rotating speed is expressed in rpm [30, 31].

For the rotating ring-disk electrode (RRDE) measurements, the catalyst ink and electrode were prepared by the same method as for those with the RDE. The disk electrode was scanned at a rate of 5 $mV{\cdot}s^{-1}$, and the ring potential was constant at 1.3 V vs. RHE. The production percentage of the HO_2^- intermediate ($\%HO_2^-$) and the electron transfer number (n) were determined by the following equations [32, 33]

$$\%HO_2^- = \frac{200I_r}{NI_d + I_r} \quad (3)$$

$$n = \frac{4NI_d}{NI_d + I_r} \quad (4)$$

where I_d is the disk current, I_r is the ring current, and N is the current collection efficiency of the Pt ring, which was determined to be 0.37.

2.4 Instruments

The phase purity and crystallinity of the products

were identified by X-ray powder diffraction (XRD) on a Rigaku MiniFlex 600 I diffractometer with Cu Kα radiation (λ = 0.15406 nm). X-ray photoelectron spectroscopy (XPS) was carried out on a Thermo VG Scientific ESCALAB 250 spectrometer with an Al Kα light source. The binding energy was calibrated relative to the C 1s peak energy at 284.6 eV. The Raman spectra were recorded on a Raman spectrometer (LabRAM HR800, λ = 514 nm). The morphology and structure of the samples were investigated by scanning electron microscopy (SEM, Hitachi S5500) and transmission electron microscopy (TEM, JEOL JEM-2010F, 200 kV). Thermogravimetric analysis (TGA) was carried out under a flow of air with a temperature ramp of 10 ℃·min^{-1} using a thermogravimetric analyzer (Netzsch STA 449C). The Brunauer–Emmett–Teller (BET) specific surface area was measured at 77 K using a Micromeritics ASAP 2050 system. The electrical conductivity was assessed by the four-probe method using a sourcemeter (Model 2400, Keithley) and then calculated using the equations for the bulk material below. The distance between each two probes was set at 1 mm. S_1 refers to the distance between probes 1 and 2, S_2 to the distance between probes 2 and 3, and S_3 to the distance between probes 3 and 4.

$$\rho = \frac{V}{I}C \tag{5}$$

$$C = \frac{20}{\frac{1}{S_1} + \frac{1}{S_2} - \frac{1}{S_1 + S_2} - \frac{1}{S_2 + S_3}} \tag{6}$$

3 Results and discussion

3.1 Characterization of the samples

The synthetic procedure for the porous $MnCo_2O_4$/C nanosheets is shown in Scheme 1 by a series of idealized models. Step I consists in dissolving and precipitating a Mn^{2+}/Co^{2+}–$C_6H_{12}O_6$-coated NaCl hybrid from a mixed solution of $Mn(Ac)_2$, $Co(Ac)_2$, and $C_6H_{12}O_6$. Cubic NaCl was selected as the template as it is less soluble than the metal precursors and glucose in water, and thus tends to precipitate before the metal precursors and glucose during recrystallization, acting as a solid synthetic template at the pyrolysis

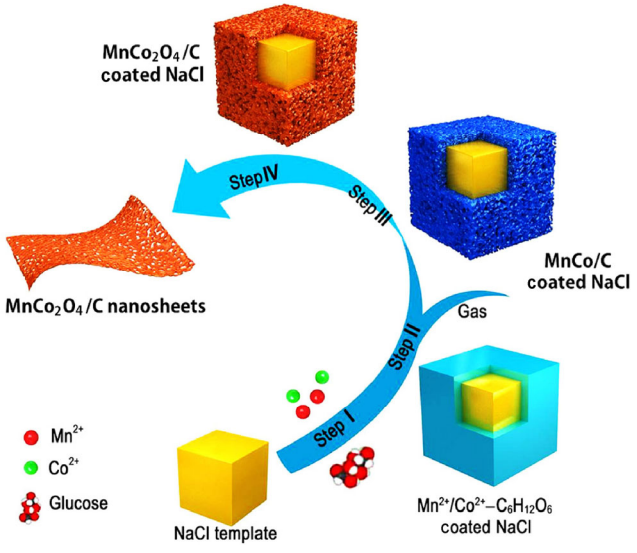

Scheme 1 Schematic of the formation of the porous $MnCo_2O_4$/C nanosheets. (Step I) Formation of the Mn^{2+}/Co^{2+}–$C_6H_{12}O_6$ coated NaCl hybrid. (Step II) Formation of the MnCo/C-coated NaCl hybrid. (Step III) Formation of the $MnCo_2O_4$/C-coated NaCl hybrid. (Step IV) Formation of the porous $MnCo_2O_4$/C nanosheets.

stage. Step II involves the formation of the metal oxide by thermal decomposition of the inorganic metal salts, and the subsequent reduction by glucose carbonization under Ar gas, leading to the formation of the MnCo/C-coated NaCl hybrid (Fig. S1 in the Electronic Supplementary Material (ESM)). Due to the release of gases during pyrolysis, a porous nanostructure is effectively obtained (Fig. S2, ESM). In step III, the MnCo/C-coated NaCl hybrid is further calcined in air (300 ℃) to oxidize MnCo/C and form the $MnCo_2O_4$/C-coated NaCl hybrid. Finally, the obtained powder is treated with deionized water/ethanol to remove the NaCl, and porous $MnCo_2O_4$/C nanosheets are obtained. During the synthetic process, the presence of NaCl plays an essential role in the formation of 2D nanosheets. Without the NaCl template, only micron-size carbon blocks are obtained (Fig. S3, ESM). The surface of water-soluble cubic NaCl can be effectively used as a template for the synthesis of 2D nanosheets, which is consistent with other recent reports [34, 35]. The synthetic strategy outlined here is highly attractive for practical applications owing to its low cost, environmental benignancy, and the possibility for large-scale production.

The XRD pattern in Fig. 1(a) shows that the diffraction peaks of the face centered cubic spinel $MnCo_2O_4$ phase

(space group *Fd*3*m* (227), JCPDS No. 23-1237) and carbon (marked with asterisks) coexist in the obtained product. No noticeable impurity phases can be detected in the sample. These experimental data confirm that MnCo/C is oxidized and completely transformed into a $MnCo_2O_4$/C hybrid after thermal treatment at 300 °C for 4 h in air. This $MnCo_2O_4$ spinel is regarded as a mixed valence oxide that adopts a structure in which Mn and Co ions are distributed over octahedral and tetrahedral stacking interstices (Fig. 1(a), inset). Regarding carbon in the $MnCo_2O_4$/C hybrid, the interlayer distance (*d*) obtained from the (002) peaks is around 0.344 nm ($d_{graphite}$ = 0.335 nm), indicating that the carbon in the $MnCo_2O_4$/C hybrid has a well-developed graphitic structure [36–38]. The Raman spectrum exhibits the characteristic D and G bands for the $MnCo_2O_4$/C hybrid at 1,343 and 1,600 cm^{-1}, respectively (Fig. 1(b)). Generally, the peak intensity ratio between the G and D bands (I_G/I_D) provides an important index for the assessment of the graphitization degree of carbon materials [38–40]. The calculated I_G/I_D ratio for the $MnCo_2O_4$/C hybrid is 1.15, while that of Vulcan XC-72R carbon is 0.86. The higher I_G/I_D ratio is a clear indication of a larger number of graphene layers [38–40]. Moreover, the appearance of the characteristic peaks for the Mn–O and Co–O bonds also confirms that high-quality $MnCo_2O_4$ spinel has been successfully prepared in this study. The $MnCo_2O_4$ loading in the as-prepared $MnCo_2O_4$/C hybrid was determined to be about 20.7 wt.% by TGA (Fig. S4, ESM).

The morphology and structure of the $MnCo_2O_4$/C hybrid were initially characterized by SEM. The low-resolution SEM images reveal a predominantly 2D sheet-like structure with high density, and the surface of each nanosheet is full of voids (Figs. 2(a) and 2(b)). It should be noted that the 2D porous morphology of the MnCo/C hybrid is nicely maintained by the $MnCo_2O_4$/C hybrid after annealing in air, indicating that the 2D porous nanosheets are reasonably thermally stable, and present no structural collapse. The thickness of a single nanosheet was estimated to be about 38.6 nm (Fig. 2(c)). A closer look at the high-resolution SEM image reveals that the nanosheets consist of numerous interconnected nanoparticles forming a cross-linked porous architecture with a uniform pore size (Fig. 2(d)),

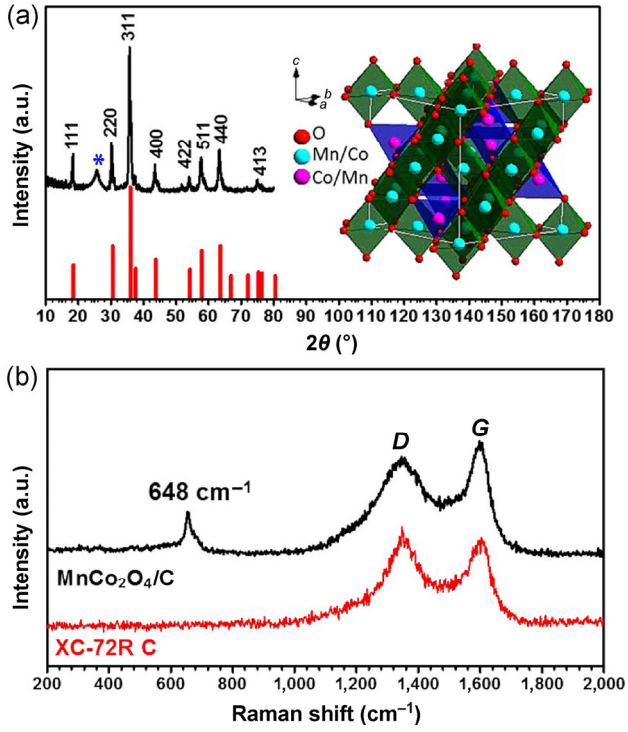

Figure 1 (a) XRD pattern of the porous $MnCo_2O_4$/C nanosheets; the inset shows the corresponding crystal structure. (b) Raman spectra of the porous $MnCo_2O_4$/C nanosheets and XC-72R carbon.

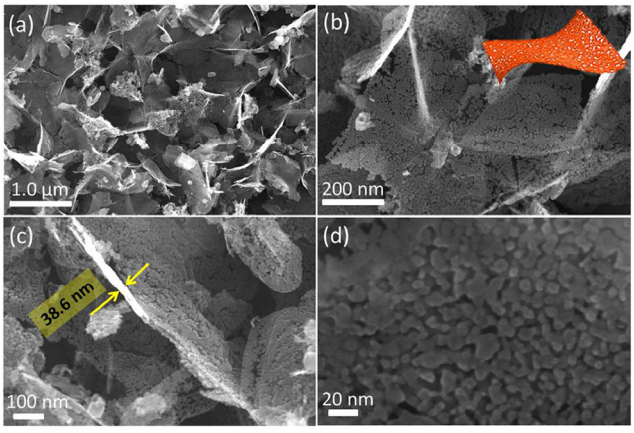

Figure 2 Morphological and structural characterization: SEM images of the porous $MnCo_2O_4$/C nanosheets at different magnifications.

as supported by the N_2 adsorption/desorption analysis (Fig. S5, ESM). The Barrett–Joyner–Halenda (BJH) pore size distribution plot (Fig. S5(b), ESM) shows a narrow pore size distribution centered at around 12.8 nm. Prompted by their porous characteristics, the $MnCo_2O_4$/C nanosheets should have a high surface area. Indeed, the BET surface area of the $MnCo_2O_4$/C nanosheets was measured to be 175.3 $m^2 \cdot g^{-1}$. The

formation of abundant pores is probably caused by the evolution of gas from both the thermal decomposition process and the carbonization process of glucose. At the same time, glucose can be turned into molten syrup, which is easily blown to form bubbles in the presence of gas and adhere to the NaCl surface, resulting in the final formation of 2D porous nanosheets [41, 42].

Such 2D sheet-like structural features are further observed clearly in the TEM images (Fig. 3(a)). As shown in Fig. 3(b) and Fig. S6 in the ESM, these nanosheets appear as a foam-like porous structure with many $MnCo_2O_4$/C nanoparticles (black spots) homogeneously embedded. Upon removal of $MnCo_2O_4$ from the porous $MnCo_2O_4$/C nanosheets with HCl, pure carbon nanosheets with a porous structure were exposed on the outside (Fig. S7, ESM). The porous carbon nanosheets present a very high graphitization degree with a layer-spacing of ~0.347 nm (Fig. S8, ESM), which is consistent with the XRD and Raman analyses. The clear fringes observed in the high-resolution TEM (HRTEM) image and the corresponding fast Fourier transform (FFT) diffraction pattern (Fig. 3(c)) indicates the high crystallinity of the $MnCo_2O_4$ nanoparticles. The interval between two lattice fringes was estimated to be around 0.479 nm (Fig. 3(c)), which is consistent with the {111} lattice spacing of the cubic spinel $MnCo_2O_4$ phase and the XRD analysis. The energy-dispersive X-ray (EDX) elemental mappings show that all the elements (Mn, Co, and O) are homogenously distributed in the carbon matrix (Fig. 3(d)). The molar ratio between Mn and Co is almost 1:2, as confirmed by the EDX spectrum, in agreement with the stoichiometric ratio of $MnCo_2O_4$ (Fig. 3(e)).

XPS analysis was performed to further investigate the surface chemical composition of the porous $MnCo_2O_4$/C nanosheets. The survey scan spectrum shows the presence of Co, Mn, C, and O elements (Fig. 4(a)). In the Co 2p spectrum (Fig. 4(b)), two major peaks are observed at binding energies of 780.08 (Co 2p3/2) and 795.23 eV (Co 2p1/2), with two weak shakeup satellite peaks. The Co 2p spectrum was fitted with the Gaussian fitting method considering the two spin–orbit doublet characteristic of Co^{2+} and Co^{3+} ions. The binding-energy separation between the two main peaks is about 15.2 eV, in line with previous reports [40, 43, 44]. Similarly, the Mn 2p3/2 and Mn 2p1/2 peaks at 642.00 and 653.51 eV, respectively, can be

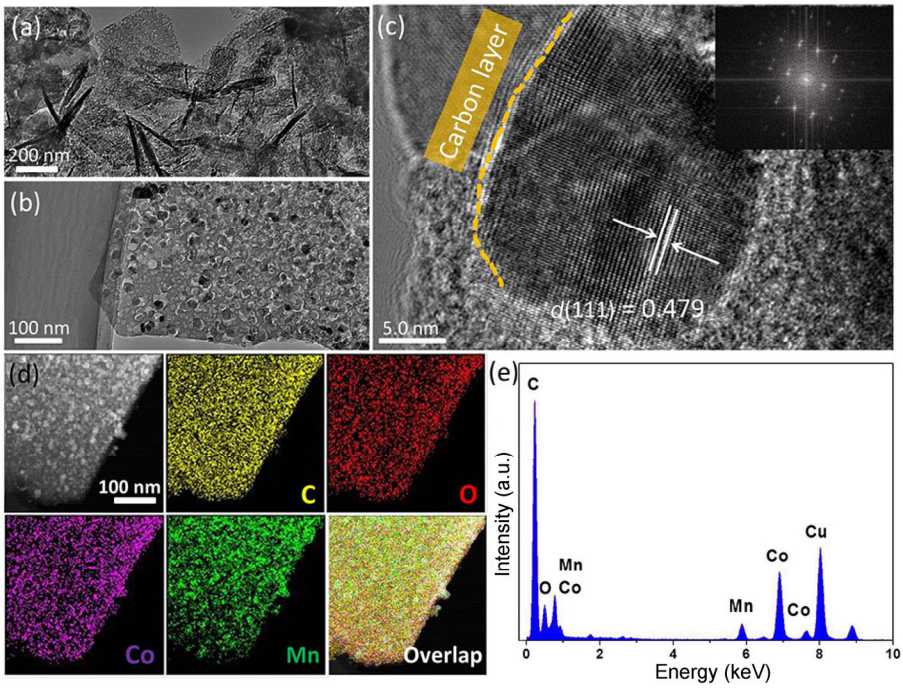

Figure 3 Morphological and elemental analysis: (a) typical TEM image, (b) magnified TEM image, (c) HRTEM image, (d) EDX elemental mappings, and (e) EDX spectrum of the porous $MnCo_2O_4$/C nanosheets. The inset in (c) shows the corresponding FFT pattern.

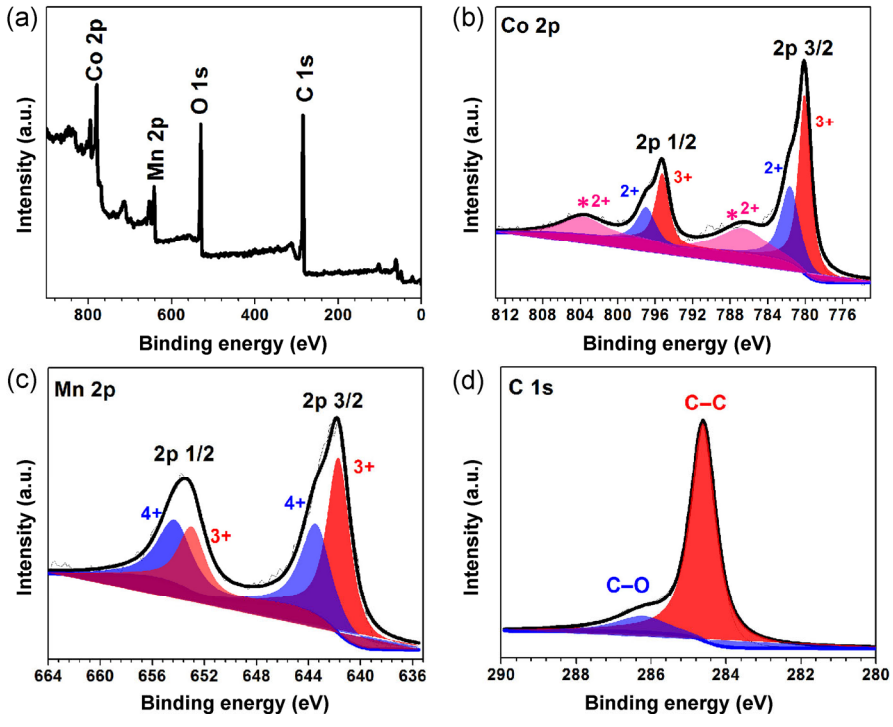

Figure 4 XPS spectra of the $MnCo_2O_4$/C nanosheets: (a) survey scan spectrum. High-resolution spectra of (b) Mn 2p, (c) Co 2p, and (d) C 1s.

resolved into four peak components (Fig. 4(c)): The two peaks at binding energies of 641.8 and 653.3 eV are attributed to Mn^{3+} ions, whereas the other two peaks at binding energies of 644.2 and 654.7 eV are assigned to Mn^{4+} ions [40, 43, 44]. These results show that the solid-state redox couples Co^{3+}/Co^{2+} and Mn^{4+}/Mn^{3+} coexist in spinel $MnCo_2O_4$. The de-convoluted C 1s spectrum of the $MnCo_2O_4$/C nanosheets is also presented in Fig. 4(d). The C 1s peak shows prominent non-oxygenated carbon species (C–C) at 284.8 eV, indicating that activated carbon exists in the $MnCo_2O_4$/C nanosheets. Obviously, the presence of activated carbon is advantageous for the conductivity of the active material. The electrical conductivity of the $MnCo_2O_4$/C nanosheets was measured to be 1.15×10^2 S·cm^{-1}. Additionally, a fraction of C atoms is observed to contain oxygen functionalities, which may be derived from covalent coupling between the spinel and some carbon atoms or from oxygen-containing groups formed on the carbon surface after pyrolysis (Step III). Overall, the as-prepared $MnCo_2O_4$/C nanosheets present the combined properties of an interconnected porous structure and a large surface area, as well as good conductivity. Thus, the $MnCo_2O_4$/C nanosheets can offer structural advantages as O_2 electrode catalysts: (i) The interconnected porous structure provides abundant catalytically active sites for the transmission of the reactant and resultant molecules throughout the catalyst and, accordingly, the inner catalysts can efficiently participate in electrocatalytic reactions; and (ii) the existence of graphitic carbon in the composites can satisfactorily overcome the poor electrical conductivity of $MnCo_2O_4$ as a result of the high conductivity of graphitic carbon and, accordingly, the $MnCo_2O_4$/C nanosheets display the required electrical conductivity from an electrocatalyst to promote oxidation reduction reactions [23, 40, 45].

3.2 Electrochemical measurements

The electrocatalytic activity of $MnCo_2O_4$/C nanosheets for the ORR was first characterized by cyclic voltammetry (CV) in a 0.1 M KOH solution on a glassy carbon electrode (Fig. 5(a)). For comparison, pure $MnCo_2O_4$ nanoparticles, carbon nanosheets, and Vulcan XC-72R carbon were also evaluated as catalysts via the same procedure. As expected, pure $MnCo_2O_4$ nanoparticles display certain ORR catalytic activity, but with a poor onset potential and peak potential.

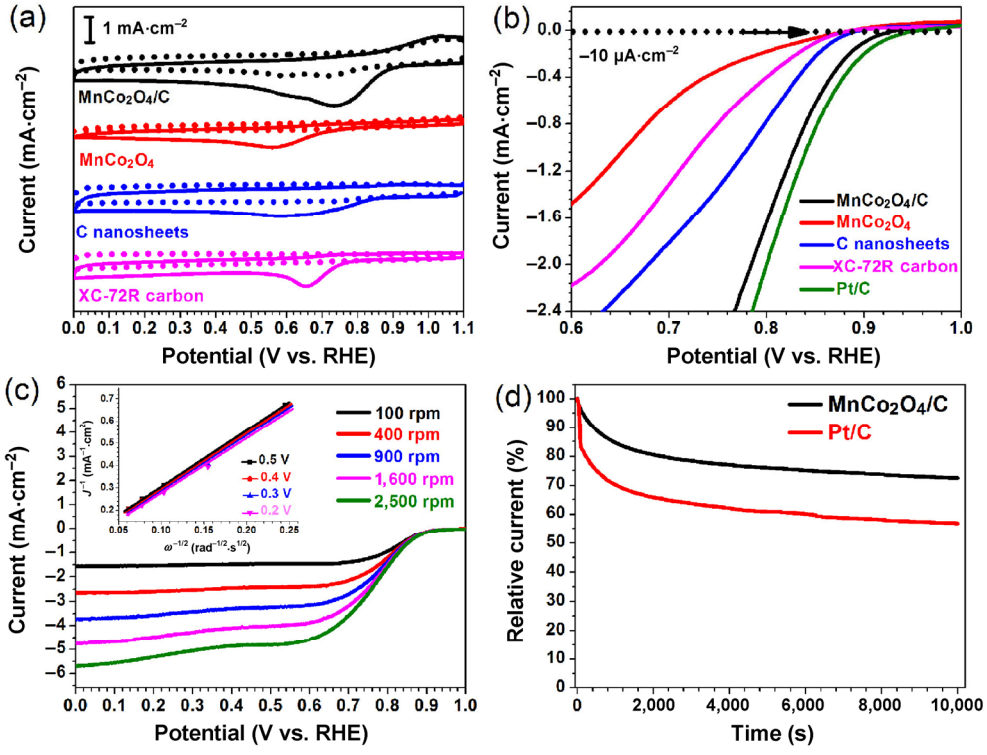

Figure 5 (a) CV curves of the porous $MnCo_2O_4$/C nanosheets, pure $MnCo_2O_4$, C nanosheets, and XC-72R carbon on glassy carbon electrodes in a N_2-saturated (dashed line) or O_2-saturated (solid line) 0.1 M KOH solution. (b) LSV curves of the $MnCo_2O_4$/C nanosheets, pure $MnCo_2O_4$, C nanosheets, XC-72R carbon, and Pt/C in an O_2-saturated 0.1 M KOH solution at a sweep rate of 5 $mV \cdot s^{-1}$ at 1,600 rpm. (c) LSV curves of the $MnCo_2O_4$/C nanosheets in an O_2-saturated 0.1 M KOH solution at different rotation speeds. Scan rate: 5 $mV \cdot s^{-1}$. The inset shows the corresponding Koutecky–Levich plots for the $MnCo_2O_4$/C nanosheets at different potentials. (d) Chronoamperometric responses of the $MnCo_2O_4$/C nanosheets and Pt/C at 0.6 V vs. RHE in an O_2-saturated 0.1 M KOH solution.

After decoration with carbon, the $MnCo_2O_4$/C nanosheets exhibit a pronounced ORR activity associated with a more positive onset potential and higher cathodic current density than those of pure $MnCo_2O_4$ nanoparticles, suggesting a synergistic effect between $MnCo_2O_4$ and the carbon nanosheets. Meanwhile, the ORR activity of the carbon nanosheets is superior to that of XC-72R carbon, which may be attributed to its porous characteristics and high graphitization degree. To gain insight into the ORR process on the materials, linear sweep voltammograms (LSVs) were recorded in an O_2-saturated 0.1 M KOH solution using an RDE (Fig. 5(b)). Similar trends for the ORR activity were observed in the RDE measurements using the electrocatalysts (Fig. 5(b) and Fig. S9 in the ESM). The onset potential for the ORR, which is defined as the potential corresponding to −10 $\mu A \cdot cm^{-2}$, was used as an indicator of ORR activity [46]. It is worth noting that the $MnCo_2O_4$/C nanosheets show a very positive onset potential (0.945 V vs. RHE), close to that of the Pt/C catalyst (0.951 V vs. RHE) (Fig. 5(b)), and the half-wave potential difference between the $MnCo_2O_4$/C nanosheets (0.767 V vs. RHE) and Pt/C (0.801 V vs. RHE) is only 34 mV at the same mass loading (Fig. S9, ESM). The obtained onset potential value for the $MnCo_2O_4$/C nanosheets is comparable to that of high-performance non-noble metal catalysts such as $MnCo_2O_4$/N-doped carbon nanotubes (CNTs) [47], Co_3O_4/graphene [18], $NiCo_2O_4$/reduced graphene oxide [48], NiT/carbon spheres-Fe_3O_4 [49], Mn_xO_y/nitrogen-doped carbon (NC) and Co_xO_y/NC composite materials [50]. Additionally, the $MnCo_2O_4$/C nanosheets exhibit a much higher ORR current density than $MnCo_2O_4$, carbon nanosheets, and XC-72R carbon, and a comparable one to that of the Pt/C catalyst (Fig. S9, ESM).

Figure 5(c) shows a set of ORR polarization curves for the $MnCo_2O_4$/C nanosheets recorded on an RDE at different rotating speeds. The current increased

with the increasing rotating speed as a result of faster oxygen flux to the electrode surface. The observed rotating speed-dependent current can be theoretically expressed by the Koutecky–Levich equation for the analysis of ORR kinetics [6, 51]. The Koutecky–Levich plot is shown in the inset, from which the electron transfer number (n) of the ORR can be calculated from the slope of the fitted lines. Based on the average values calculated at different potentials, n was calculated to be 3.82, demonstrating that the $MnCo_2O_4$/C nanosheets favor the desirable four-electron transfer pathway. This agrees well with recent reports regarding other transition metal oxides [17–19, 51, 52]. RRDE measurements were further conducted to verify the ORR pathway in the $MnCo_2O_4$/C nanosheets (Fig. S10(a), ESM). The HO_2^- yield and the electron transfer number n were calculated from the corresponding disk and ring currents (Fig. S10(b), ESM). The ORR on the $MnCo_2O_4$/C nanosheets yielded about 8.4%–17.0% HO_2^- over the potential range from 0.2 to 0.7 V, with n ranging from 3.66 to 3.83, indicative of a dominant four-electron reduction process, which is in agreement with the result obtained from the Koutecky–Levich plots based on the RDE measurements. In addition, the $MnCo_2O_4$/C nanosheets also exhibit excellent stability compared to the Pt/C catalyst, as measured by chronoamperometric measurements (Fig. 5(d)). After 10,000 s of continuous operation, the ORR current density of the $MnCo_2O_4$/C nanosheets at 0.60 V decreased by just 27.5%, while the corresponding Pt/C catalyst exhibited a 43% decrease in the current density in the same period.

The superior ORR performance of the $MnCo_2O_4$/C nanosheets possibly arises from the following factors: (i) Its unique 2D porous architecture with a high BET surface area provides more active sites for the ORR catalysis, and the large pore volume facilitates oxygen and electrolyte transport to the active sites. (ii) The catalytic coupling effect between $MnCo_2O_4$ and graphitic carbon may play a positive role in enhancing the ORR performance [49, 53]. The coupling effect between $MnCo_2O_4$ and carbon is evident from the binding energy shifts for Mn and Co in the samples with and without carbon. As shown in Fig. S11(a) (see ESM), the Mn 2p3/2 binding energy of the $MnCo_2O_4$/C nanosheets shifts to a higher value with respect to that of pure $MnCo_2O_4$. The positive peak shift is also pronounced for the Co cations, as reflected in Fig. S11(b) in the ESM. The integration of $MnCo_2O_4$ within the carbonaceous structure promotes the formation of a conducting network, facilitating the charge transfer during the ORR at the oxide surface [17–19, 51, 52]. (iii) In addition, the XPS results shown in Fig. 4 indicate that the solid-state redox couples Mn^{4+}/Mn^{3+} and Co^{3+}/Co^{2+} coexist in the spinel $MnCo_2O_4$, which provide a significant number of catalytically active sites [17, 44, 54, 55]. Note that Mn^{3+}/Mn^{4+} species are considered to be more active than Co species [54, 55].

In order to investigate the optimal $MnCo_2O_4$ content in the $MnCo_2O_4$/C hybrids for the best catalytic activity, two other $MnCo_2O_4$/C catalysts with different $MnCo_2O_4$ content were prepared. The amount of $MnCo_2O_4$ on carbon was controlled by varying the glucose content. The amount of glucose was set to be 1.0 and 4.0 g, for which the samples were named $MnCo_2O_4$/C-1.0 and $MnCo_2O_4$/C-4.0, respectively. The morphology, crystal structure, and composition of the two samples were characterized by TEM, XRD, and TGA; the detailed analysis results are shown in Fig. S12 in the ESM. According to the TGA curves (Fig. S12(d), ESM), the content of $MnCo_2O_4$ was estimated to be about 43.9 wt.% for $MnCo_2O_4$/C-1.0, and 9.6 wt.% for $MnCo_2O_4$/C-4.0. We observed that the $MnCo_2O_4$/C nanosheet sample exhibits the most positive onset potential and the highest current density among all the samples (Fig. S13, ESM), demonstrating that the $MnCo_2O_4$/C nanosheet catalyst displays the best ORR performance. Based on the TEM analysis (see Figs. S12(a) and S12(b) in the ESM for details), we can speculate that the very low loading of $MnCo_2O_4$ particles in the $MnCo_2O_4$/C-4.0 sample generates fewer ORR active sites, whereas the excessively high loading in $MnCo_2O_4$/C-1.0 results in the aggregation of the particles and a low catalytic activity. In addition, spinel $MnCo_2O_4$ has a much lower electrical conductivity than carbon materials, which may limit electron transport on its catalytically active sites. Thus, $MnCo_2O_4$/C-1.0 displays the lowest current density among all samples due to its low carbon content.

For practical applications, the resistance of the catalysts toward alcohol crossover effects is an important consideration [27, 28, 48]. Thus, the electrocatalytic

selectivity of the $MnCo_2O_4$/C nanosheets against methanol oxidation was studied. After the addition of methanol, no noticeable changes in the oxygen reduction current were observed for the $MnCo_2O_4$/C nanosheets, although the reduction peak center slightly shifted to a lower potential (Fig. 6(a)). In contrast, the commercial Pt/C catalyst showed the typical methanol oxidation peaks at potentials of 0.70 and 0.77 V in the positive and negative CV scans, respectively (Fig. 6(b)), indicating that Pt/C is very sensitive to methanol crossover. The results demonstrate that the $MnCo_2O_4$/C nanosheets possess high selectivity for the ORR, which is a valuable feature for practical applications.

4 Conclusions

In summary, we have developed a low-cost and effective way to obtain a porous sheet-like $MnCo_2O_4$/C electrocatalyst by a NaCl template-directed pyrolysis approach using glucose as the carbon source. The synthesized porous $MnCo_2O_4$/C nanosheets exhibit superior electrochemical characteristics for the ORR in alkaline medium. The porous structure and large surface area, together with a good electrical conductivity are responsible for the prominently enhanced electrochemical performance of the $MnCo_2O_4$/C nanosheets. Remarkably, the $MnCo_2O_4$/C nanosheets present an ORR onset potential of 0.945 V vs. RHE close to that of a commercial Pt/C catalyst (0.951 vs. RHE), suggesting its promising application as an efficient ORR catalyst in electrochemical energy storage and conversion devices.

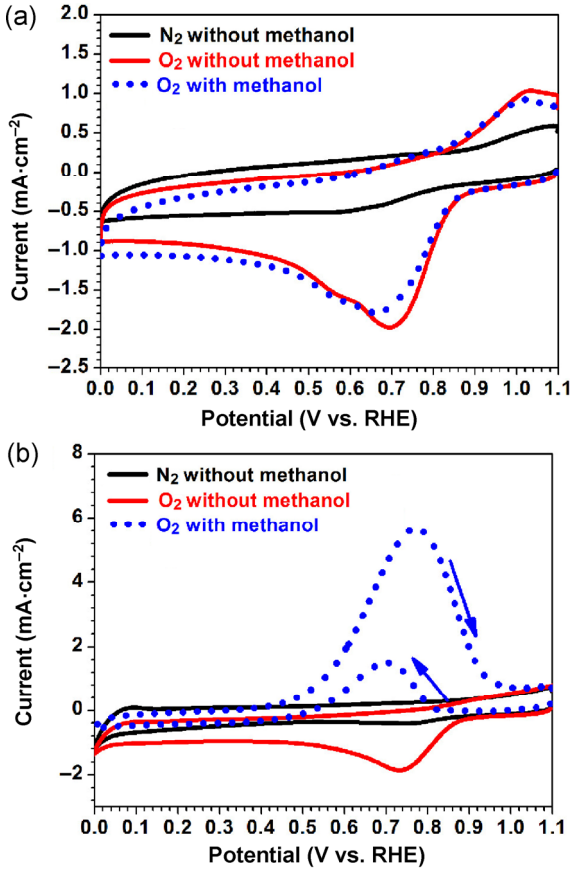

Figure 6 CV curves of (a) the $MnCo_2O_4$/C nanosheets and (b) Pt/C in 0.1 M KOH solution with and without 0.5 M methanol at a scan rate of 10 $mV \cdot s^{-1}$.

Acknowledgements

The authors acknowledge the National Natural Science Foundation of China (Nos. 21576139, 21503111, 21376122, and 21273116), Jiangsu Provincial Natural Science Foundation of Jiangsu Province (No. BK20140926), Specialized Research Fund for the Doctoral Program of Higher Education (No. 20130202120010), the Key Science and Technology Program of Shaanxi Province, China (No. 2014K10-06), Fundamental Research Funds for the Central Universities (No. GK201503038), China Scholarship Council (CSC, 201506860013), University Postgraduate Research and Innovation Project in Jiangsu Province (No. KYZZ15_0213), National and Local Joint Engineering Research Center of Biomedical Functional Material, and a project funded by the Priority Academic Program Development of Jiangsu Higher Education Institutions. The authors also thank John B. Goodenough of the university of Texas at Austin for his support and help.

Electronic Supplementary Material: Supplementary material (experimental details, additional SEM and TEM images, N_2 adsorption–desorption isotherms, XRD, XPS, and TGA patterns, and linear sweep voltammogram results) is available in the online version of this article at http://dx.doi.org/10.1007/s12274-016-1101-2.

References

[1] Stambouli, A. B.; Traversa, E. Fuel cells, an alternative to standard sources of energy. *Renew. Sust. Energ. Rev.* **2002**, *6*, 295–304.

[2] Carrette, L.; Friedrich, K. A.; Stimming, U. Fuel cells: Principles, types, fuels, and applications. *ChemPhysChem* **2000**, *1*, 162–193.

[3] Bashyam, R.; Zelenay, P. A class of non-precious metal composite catalysts for fuel cells. *Nature* **2006**, *443*, 63–66.

[4] Feng, J.; Liang, Y. Y.; Wang, H. L.; Li, Y. G.; Zhang, B.; Zhou, J. G.; Wang, J.; Regier, T.; Dai, H. J. Engineering manganese oxide/nanocarbon hybrid materials for oxygen reduction electrocatalysis. *Nano Res.* **2012**, *5*, 718–725.

[5] Huang, D. K.; Luo, Y. P.; Li, S. H.; Zhang, B. Y.; Shen, Y.; Wang, M. K. Active catalysts based on cobalt oxide@cobalt/N-C nanocomposites for oxygen reduction reaction in alkaline solutions. *Nano Res.* **2014**, *7*, 1054–1064.

[6] Yamamoto, K.; Imaoka, T.; Chun, W.-J.; Enoki, O.; Katoh, H.; Takenaga, M.; Sonoi, A. Size-specific catalytic activity of platinum clusters enhances oxygen reduction reactions. *Nat. Chem.* **2009**, *1*, 397–402.

[7] Debe, M. K. Electrocatalyst approaches and challenges for automotive fuel cells. *Nature* **2012**, *486*, 43–51.

[8] Cao, T.; Wang, D. S.; Zhang, J. T.; Cao, C. B.; Li, Y. D. Bamboo-like nitrogen-doped carbon nanotubes with Co nanoparticles encapsulated at the tips: Uniform and large-scale synthesis and high-performance electrocatalysts for oxygen reduction. *Chem.—Eur. J.* **2015**, *21*, 14022–14029.

[9] Shi, H.; Shen, Y. F.; He, F.; Li, Y.; Liu, A. R.; Liu, S. Q.; Zhang, Y. J. Recent advances of doped carbon as non-precious catalysts for oxygen reduction reaction. *J. Mater. Chem. A* **2014**, *2*, 15704–15716.

[10] Zhang, Y. J.; Fugane, K.; Mori, T.; Niu, L.; Ye, J. H. Wet chemical synthesis of nitrogen-doped graphene towards oxygen reduction electrocatalysts without high-temperature pyrolysis. *J. Mater. Chem.* **2012**, *22*, 6575–6580.

[11] Tahir, M.; Mahmood, N.; Zhang, X. X.; Mahmood, T.; Butt, F. K.; Aslam, I.; Tanveer, M.; Idrees, F.; Khalid, S.; Shakir, I. et al. Bifunctional catalysts of Co_3O_4@GCN tubular nanostructured (TNS) hybrids for oxygen and hydrogen evolution reactions. *Nano Res.* **2015**, *8*, 3725–3736.

[12] Ma, Z. L.; Dou, S.; Shen, A. L.; Tao, L.; Dai, L. M.; Wang, S. Y. Sulfur-doped graphene derived from cycled lithium–sulfur batteries as a metal-free electrocatalyst for the oxygen reduction reaction. *Angew. Chem., Int. Ed.* **2015**, *127*, 1908–1912.

[13] Żółtowski, P.; Dražić, D. M.; Vorkapić, L. Carbon-air electrode with regenerative short time overload capacity: Part 1. Effect of manganese dioxide. *J. Appl. Electrochem.* **1973**, *3*, 271–283.

[14] Bragg, W. H. The structure of magnetite and the spinels. *Nature* **1915**, *95*, 561.

[15] Wu, J. H.; Dou, S.; Shen, A. L.; Wang, X.; Ma, Z. L.; Ouyang, C. B.; Wang, S. Y. One-step hydrothermal synthesis of $NiCo_2S_4$–rGO as an efficient electrocatalyst for the oxygen reduction reaction. *J. Mater. Chem. A* **2014**, *2*, 20990–20995.

[16] Yang, H. C.; Hu, F.; Zhang, Y. J.; Shi, L. Y.; Wang, Q. B. Controlled synthesis of porous spinel cobalt manganese oxides as efficient oxygen reduction reaction electrocatalysts. *Nano Res.* **2016**, *9*, 207–213.

[17] Liang, Y. Y.; Wang, H. L.; Zhou, J. G.; Li, Y. G.; Wang, J.; Regier, T.; Dai, H. J. Covalent hybrid of spinel manganese–cobalt oxide and graphene as advanced oxygen reduction electrocatalysts. *J. Am. Chem. Soc.* **2012**, *134*, 3517–3523.

[18] Liang, Y. Y.; Li, Y. G.; Wang, H. L.; Zhou, J. G.; Wang, J.; Regier, T.; Dai, H. J. Co_3O_4 nanocrystals on graphene as a synergistic catalyst for oxygen reduction reaction. *Nat. Mater.* **2011**, *10*, 780–786.

[19] Li, C.; Han, X. P.; Cheng, F. Y.; Hu, Y. X.; Chen, C. C.; Chen, J. Phase and composition controllable synthesis of cobalt manganese spinel nanoparticles towards efficient oxygen electrocatalysis. *Nat. Commun.* **2015**, *6*, 7345.

[20] Zhu, C. Z.; Du, D.; Eychmüller, A.; Lin, Y. H. Engineering ordered and nonordered porous noble metal nanostructures: Synthesis, assembly, and their applications in electrochemistry. *Chem. Rev.* **2015**, *115*, 8896–8943.

[21] Walcarius, A. Mesoporous materials and electrochemistry. *Chem. Soc. Rev.* **2013**, *42*, 4098–4140.

[22] Xu, Y.; Zhang, B. Recent advances in porous Pt-based nanostructures: Synthesis and electrochemical applications. *Chem. Soc. Rev.* **2014**, *43*, 2439–2450.

[23] Zhu, C. Z.; Li, H.; Fu, S. F.; Du, D.; Lin, Y. H. Highly efficient nonprecious metal catalysts towards oxygen reduction reaction based on three-dimensional porous carbon nanostructures. *Chem. Soc. Rev.* **2016**, *45*, 517–531.

[24] Ji, Y. J.; Wu, Y.; Zhao, G. F.; Wang, D. S.; Liu, L.; He, W.; Li, Y. D. Porous bimetallic Pt-Fe nanocatalysts for highly efficient hydrogenation of acetone. *Nano Res.* **2015**, *8*, 2706–2713.

[25] Cao, X. C.; Wu, J.; Jin, C.; Tian, J. H.; Strasser, P.; Yang, R. Z. $MnCo_2O_4$ anchored on P-doped hierarchical porous carbon as an electrocatalyst for high-performance rechargeable Li–O_2 batteries. *ACS Catal.* **2015**, *5*, 4890–4896.

[26] Xu, Y. J.; Tsou, A.; Fu, Y.; Wang, J.; Tian, J.-H.; Yang, R. Z. Carbon-coated perovskite $BaMnO_3$ porous nanorods with enhanced electrocatalytic perporites for oxygen reduction and oxygen evolution. *Electrochim. Acta* **2015**, *174*, 551–556.

[27] Lee, J. S.; Park, G. S.; Kim, S. T.; Liu, M. L.; Cho, J. A highly efficient electrocatalyst for the oxygen reduction

reaction: N-doped ketjenblack incorporated into Fe/Fe_3C-functionalized melamine foam. *Angew. Chem., Int. Ed.* **2013**, *125*, 1060–1064.

[28] Cong, H.-P.; Wang, P.; Gong, M.; Yu, S.-H. Facile synthesis of mesoporous nitrogen-doped graphene: An efficient methanol–tolerant cathodic catalyst for oxygen reduction reaction. *Nano Energy* **2014**, *3*, 55–63.

[29] Bard, A. J.; Faulkner, L. R. *Electrochemical Methods: Fundamentals and Applications*; Wiley: New York, 1980.

[30] Gao, S. Y.; Geng, K. R. Facile construction of Mn_3O_4 nanorods coated by a layer of nitrogen-doped carbon with high activity for oxygen reduction reaction. *Nano Energy* **2014**, *6*, 44–50.

[31] Du, C. C.; Huang, H.; Feng, X.; Wu, S. Y.; Song, W. B. Confining MoS_2 nanodots in 3D porous nitrogen-doped graphene with amendable ORR performance. *J. Mater. Chem. A* **2015**, *3*, 7616–7622.

[32] Li, R.; Wei, Z. D.; Gou, X. L. Nitrogen and phosphorus dual-doped graphene/carbon nanosheets as bifunctional electrocatalysts for oxygen reduction and evolution. *ACS Catal.* **2015**, *5*, 4133–4142.

[33] Jung, J. I.; Jeong, H. Y.; Lee, J. S.; Kim, M. G.; Cho, J. A bifunctional perovskite catalyst for oxygen reduction and evolution. *Angew. Chem., Int. Ed.* **2014**, *126*, 4670–4674.

[34] Xu, Y. X.; Li, W. Y.; Zhang, F.; Zhang, X. L.; Zhang, W. J.; Lee, C.-S.; Tang, Y. B. *In situ* incorporation of FeS nanoparticles/carbon nanosheets composite with an interconnected porous structure as a high-performance anode for lithium ion batteries. *J. Mater. Chem. A* **2016**, *4*, 3697–3703.

[35] Li, W. Y.; Tang, Y. B.; Kang, W. P.; Zhang, Z. Y.; Yang, X.; Zhu, Y.; Zhang, W. J.; Lee, C. S. Core–shell Si/C nanospheres embedded in bubble sheet-like carbon film with enhanced performance as lithium ion battery anodes. *Small* **2015**, *11*, 1345–1351.

[36] Kang, E.; Jung, Y. S.; Cavanagh, A. S.; Kim, G. H.; George, S. M.; Dillon, A. C.; Kim, J. K.; Lee, J. Fe_3O_4 nanoparticles confined in mesocellular carbon foam for high performance anode materials for lithium-ion batteries. *Adv. Funct. Mater.* **2011**, *21*, 2430–2438.

[37] Chen, L.; Wang, Z. Y.; He, C. N.; Zhao, N. Q.; Shi, C. S.; Liu, E. Z.; Li, J. J. Porous graphitic carbon nanosheets as a high-rate anode material for lithium-ion batteries. *ACS Appl. Mater. Interfaces* **2013**, *5*, 9537–9545.

[38] He, C. N.; Wu, S.; Zhao, N. Q.; Shi, C. S.; Liu, E. Z.; Li, J. J. Carbon-encapsulated Fe_3O_4 nanoparticles as a high-rate lithium ion battery anode material. *ACS Nano* **2013**, *7*, 4459–4469.

[39] Zhao, L.; Wang, L.; Yu, P.; Zhao, D. D.; Tian, C. G.; Feng, H.; Ma, J.; Fu, H. G. A chromium nitride/carbon nitride containing graphitic carbon nanocapsule hybrid as a Pt-free electrocatalyst for oxygen reduction. *Chem. Commun.* **2015**, *51*, 12399–12402.

[40] Kim, J. G.; Kim, Y.; Noh, Y.; Kim, W. B. $MnCo_2O_4$ nanowires anchored on reduced graphene oxide sheets as effective bifunctional catalysts for Li–O_2 battery cathodes. *ChemSusChem* **2015**, *8*, 1752–1760.

[41] Zhou, Y. S.; Chen, G.; Yu, Y. G.; Yan, C. S.; Sun, J. X.; He, F. Synthesis of metal oxide nanosheets through a novel approach for energy applications. *J. Mater. Chem. A* **2016**, *4*, 781–784.

[42] Wang, X. B.; Zhang, Y. J.; Zhi, C. Y.; Wang, X.; Tang, D. M.; Xu, Y. B.; Weng, Q. H.; Jiang, X. F.; Mitome, M.; Golberg, D. et al. Three-dimensional strutted graphene grown by substrate-free sugar blowing for high-power-density supercapacitors. *Nat. Commun.* **2013**, *4*, 2905.

[43] Oh, D.; Qi, J. J.; Han, B. H.; Zhang, G. R.; Carney, T. J.; Ohmura, J.; Zhang, Y.; Shao-Horn, Y.; Belcher, A. M. M13 virus-directed synthesis of nanostructured metal oxides for lithium–oxygen batteries. *Nano Lett.* **2014**, *14*, 4837–4845.

[44] Ge, X. M.; Liu, Y. Y.; Goh, F. W. T.; Hor, T. S. A.; Zong, Y.; Xiao, P.; Zhang, Z.; Lim, S. H.; Li, B.; Wang, X. et al. Dual-phase spinel $MnCo_2O_4$ and spinel $MnCo_2O_4$/nanocarbon hybrids for electrocatalytic oxygen reduction and evolution. *ACS Appl. Mater. Interfaces* **2014**, *6*, 12684–12691.

[45] Liang, J.; Zhou, R. F.; Chen, X. M.; Tang, Y. H.; Qiao, S. Z. Fe–N decorated hybrids of CNTs grown on hierarchically porous carbon for high-performance oxygen reduction. *Adv. Mater.* **2014**, *26*, 6074–6079.

[46] Fu, G. T.; Wu, K.; Lin, J.; Tang, Y. W.; Chen, Y.; Zhou, Y. M.; Lu, T. H. One-pot water-based synthesis of Pt–Pd alloy nanoflowers and their superior electrocatalytic activity for the oxygen reduction reaction and remarkable methanol-tolerant ability in acid media. *J. Phys. Chem. C* **2013**, *117*, 9826–9834.

[47] Zhao, A. Q.; Masa, J.; Xia, W.; Maljusch, A.; Willinger, M.-G.; Clavel, G.; Xie, K. P.; Schlögl, R.; Schuhmann, W.; Muhler, M. Spinel Mn–Co oxide in N-doped carbon nanotubes as a bifunctional electrocatalyst synthesized by oxidative cutting. *J. Am. Chem. Soc.* **2014**, *136*, 7551–7554.

[48] Zhang, G. Q.; Xia, B. Y.; Wang, X.; Lou, X. W. Strongly coupled $NiCo_2O_4$-rGO hybrid nanosheets as a methanol-tolerant electrocatalyst for the oxygen reduction reaction. *Adv. Mater.* **2014**, *26*, 2408–2412.

[49] Xia, X. H.; Wang, Y. D.; Wang, D. H.; Zhang, Y. Q.; Fan, Z. X.; Tu, J. P.; Zhang, H.; Fan, H. J. Atomic-layer-deposited iron oxide on arrays of metal/carbon spheres and their application for electrocatalysis. *Nano Energy* **2016**, *20*, 244–253.

[50] Masa, J.; Xia, W.; Sinev, I.; Zhao, A. Q.; Sun, Z. Y.; Grützke, S.; Weide, P.; Muhler, M.; Schuhmann, W. Mn_xO_y/NC and Co_xO_y/NC nanoparticles embedded in a nitrogen-doped carbon matrix for high-performance bifunctional oxygen electrodes. *Angew. Chem., Int. Ed.* **2014**, *53*, 8508–8512.

[51] Cheng, F. Y.; Shen, J.; Peng, B.; Pan, Y. D.; Tao, Z. L.; Chen, J. Rapid room-temperature synthesis of nanocrystalline spinels as oxygen reduction and evolution electrocatalysts. *Nat. Chem.* **2011**, *3*, 79–84.

[52] Wang, L.; Zhao, X.; Lu, Y. H.; Xu, M. W.; Zhang, D. W.; Ruoff, R. S.; Stevenson, K. J.; Goodenough, J. B. $CoMn_2O_4$ spinel nanoparticles grown on graphene as bifunctional catalyst for lithium-air batteries. *J. Electrochem. Soc.* **2011**, *158*, A1379–A1382.

[53] Hu, Y.; Jensen, J. O.; Zhang, W.; Cleemann, L. N.; Xing, W.; Bjerrum, N. J.; Li, Q. F. Hollow spheres of iron carbide nanoparticles encased in graphitic layers as oxygen reduction catalysts. *Angew. Chem., Int. Ed.* **2014**, *53*, 3675–3679.

[54] Ma, S. C.; Sun, L. Q.; Cong, L.; Gao, X. G.; Yao, C.; Guo, X.; Tai, L. H.; Mei, P.; Zeng, Y. P.; Xie, H. M. et al. Multiporous $MnCo_2O_4$ microspheres as an efficient bifunctional catalyst for nonaqueous Li–O_2 batteries. *J. Phys. Chem. C* **2013**, *117*, 25890–25897.

[55] De Koninck, M.; Marsan, B. $Mn_xCu_{1-x}Co_2O_4$ used as bifunctional electrocatalyst in alkaline medium. *Electrochim. Acta* **2008**, *53*, 7012–7021.